Power Electronics and Drives
Volume 10(45), 2025 DOI: 10.2478/pead-2025-0027

Power Electronics and Drives

Intelligent Control and Optimal Energy Supervision for On-Grid Hybrid Renewable Generation with Flywheel Energy Storage

Research Paper

Rym Marouani*, Marwen Zaafouri, Nejib Hamrouni, Adnane Cherif

ATSSEE, Faculty of Sciences of Tunis, University of Tunis El Manar, 1068 Tunis, Tunisia

Received: 06 August, 2025; Received in the revised form: 15 October, 2025; Accepted: 21 October, 2025

Abstract: This research introduces an innovative on-grid hybrid renewable generation (OG-HRG) system characterised by its distinctive combination of three technologies: solar photovoltaic (PV), gearless permanent magnet synchronous generator (PMSG)-based wind turbines (WTs) and a flywheel energy storage system (FESS). The particularity of this system lies in its advanced incorporation of a multi-layered control approach, which merges the adaptability of fuzzy logic control (FLC), the accuracy of proportional-integral-derivative (PID) control and the resilience of sliding mode control (SMC) into a unified energy management system (EMS). This design has been specifically developed to address intermittency and maintain grid stability. Simulation outcomes validate its effectiveness, showcasing 92.3% renewable energy utilisation, minimal frequency fluctuations (±0.8%) and an 85% decrease in CO_2 emissions. This study offers a new framework for achieving high-efficiency and stable integration of renewable energy sources.

Keywords: *on-grid hybrid renewable generation • flywheel energy storage system • fuzzy logic control • sliding mode control • energy management system*

1. Introduction

The integration of renewable energy sources (RESs) in modern power systems provides a practical solution to challenges associated with energy scarcity and environmental degradation. Since wind energy and solar energy are naturally complementary, effectively combining these two sources will enhance the reliability and efficiency of the power supply while significantly reducing carbon emissions. However, the inherent intermittency of these sources introduces substantial challenges to grid stability (Luukkanen et al., 2023), frequency regulation challenges in isolated grids (Matos et al., 2025), disturbance in power quality (Lata-García et al., 2024) and inefficient capacity utilisation (Bhutto, 2024).

Traditional solutions, such as lithium-ion batteries, which have response times >100 ms (Emon et al., 2023) and gas peaker plants, provide limited efficacy in addressing these challenges due to either their slow responsiveness or their associated emissions. This gap has catalysed research into hybrid systems that incorporate inertial storage technologies. Flywheel energy storage systems (FESS) have emerged as a promising solution, offering response times <20 ms and more than 100,000 cycles of durability (Fernandez et al., 2024). These characteristics make FESS particularly effective in alleviating the impacts of high-frequency renewable intermittency while simultaneously enhancing grid synchronisation (Younsi et al., 2023).

* *Email: rym.marouani@fst.utm.tn*

Recent advancements in hybrid wind-photovoltaic (PV) systems with integrated energy storage have led to three key architectural paradigms for addressing the intermittency of RESs (Morales-García et al., 2023). The first and most prevalent approach is the centralised DC-bus system, which has demonstrated operational efficiencies between 93% and 96% due to its common DC interconnection in large-scale grid applications (Anvari-Moghaddam et al., 2025). Enhancements, such as the torque-optimised MPPT design by Baala and Bri (2020), have been shown to improve wind energy capture by 8–12 percentage points compared with traditional systems. However, this architecture is inherently limited by vulnerabilities associated with single-point failures, particularly in fault conditions that persist for >500 ms (Li et al., 2021). By contrast, decentralised AC-coupled systems offer considerable modularity through plug-and-play functionality, facilitating flexible capacity scaling, a crucial advantage for distributed generation frameworks (Shafiullah et al., 2022). According to IEEE 1547.2-2023, compliance testing reveals that these systems often exhibit total harmonic distortion (THD) levels exceeding the 2.5% threshold, underscoring the need for improved filtering solutions. This requirement typically raises capital costs by 15%–20% (I.S.C. Committee, 2016). At the forefront of technology, hybrid DC/AC layered systems integrate both approaches by leveraging DC sub-grids alongside AC-coupled FESS (Hamrouni et al., 2019).

On the contrary, recent developments in intelligent control systems have become crucial for tackling the operational issues of renewable-based microgrids that utilise FESS (Kechida et al., 2024). Contemporary control architectures often feature a hierarchical framework that includes primary droop control for regulating voltage and frequency over sub-second intervals, model predictive control (MPC) for optimising setpoints across 15–30 s periods, and energy management systems (EMSs) that coordinate storage activity with load predictions (Serat et al., 2024). Analyses indicate considerable differences in performance across various control methods: traditional proportional-integral-derivative (PID) controllers show response times ranging from 120 ms to 300 ms with a THD of 3.2%, whereas fuzzy logic systems can achieve quicker responses of 50–80 ms with a reduced THD of 2.1% (Öhrström et al., 2025). Adaptive MPC has been shown to outperform with response times of just 20–40 ms and a THD of only 1.5%. Nonetheless, three significant challenges remain in current research: first, instability during mode shifts in 0.5–2 s grid-islanding scenarios, second, conflicting demands between quick frequency response and prolonged energy arbitrage, and third, the threat of cybersecurity issues that can lead to latency spikes of up to 230 ms in compromised systems (Roumeliotis et al., 2024). New solutions appear promising, with hybrid fuzzy-MPC controllers obtaining a tracking accuracy of 98.2%, digital twin technologies cutting computational latency by 40%, and blockchain-based communication offering verification times <5 ms (Dunna et al., 2024). These innovations underscore the necessity for advanced control frameworks that can effectively manage the multi-timescale dynamics of hybrid PV-wind-flywheel systems while ensuring grid stability and cybersecurity, an area that our proposed multi-agent control system aims to address specifically.

Research on hybrid renewable energy systems (RES) has been a prominent topic in various published studies. However, many of these evaluations primarily revolve around the operational conditions of hybrid RES featuring simpler topologies. The investigations were limited to a narrow range of operational modes and utilised basic control algorithms. Xu et al. (2023) outline the classifications and architectures of hybrid RES, while the optimisation methods for the sizing of their components are discussed in Ullah et al. (2024). An analysis of systems incorporating wind, PV, supercapacitors and batteries can be found in Chakir and Tabaa (2024). Anvari-Moghaddam et al. (2025) explored hybrid RES in standalone configurations with DC loads, while other studies (Fernandez et al., 2024) focused on systems equipped with AC loads. Several articles are dedicated exclusively to the operation of hybrid RES in standalone mode neglecting the topic of energy management strategies (Al-Rawashdeh et al., 2023). Most of the research has concentrated on systems utilising a simple topology with a machine-side converter linked to a permanent magnet synchronous generator (PMSG) (Gajewski and Pieńkowski, 2016).

This research introduces an advanced intelligent control system and optimisation framework for managing energy in an on-grid hybrid renewable generation (OG-HRG), including a FESS. This paper is organised as follows: Section 2 describes the integrated architecture and provides detailed mathematical models for the PV array, wind turbine (WT) dynamics and flywheel operation. Section 3 proposes a new control framework utilising a maximum power point tracker (MPPT) based on fuzzy logic Control (FLC) algorithms and sliding mode control (SMC), along with a comprehensive seven-mode energy management strategy. In Section 4, simulation results from key operational scenarios are presented, showing the stability of the DC bus within a deviation of ±0.005 V and an impressive renewable resource utilisation efficiency of 92.3%. Finally, Section 5 discusses implications for grid integration and potential future research avenues, including hardware-in-the-loop validation opportunities.

2. Modelling of the OG-HRG

2.1. Description of the OG_HRG

The schematic diagram presented in Figure 1 depicts the architecture of the proposed OG-HRG. This system integrates a photovoltaic generator (PVG) paired with a DC–DC boost converter, a WT with a PMSG in conjunction with a machine-side AC–DC converter and a FESS integrated with an AC–DC conversion system. The primary reason for utilising a flywheel in dynamics is its exceptionally high-power density and nearly instantaneous response time, making it perfect for handling rapid fluctuations in power demand and supply.

The flywheel is ideal for high-power, rapid-cycling applications, with a lifespan exceeding 20 years and more than 100,000 charge–discharge cycles. By contrast, typical lithium-ion batteries only last about 5,000 cycles. Flywheels respond in <100 ms, providing quick grid stabilisation, and both technologies have similar round-trip efficiencies of around 90%. However, the flywheel's durability and fast power delivery make it the best choice for frequency regulation and demanding applications requiring long-term reliability.

All the components of the structure in Figure 1 are modelled by Eqs (1)–(13) and then integrated in a dynamic Simulink model (MATLAB environment).

2.2. Modelling of the PVG

The mathematical model of a PVG with N_p parallel panels and N_s series cells is shown in Eq. (1) (Xu et al., 2023) as follows:

$$I_{\mathrm{PV}} = N_p I_{ph} - N_p I_0 \cdot \left[\exp\left(\frac{V_{PV} + \frac{N_s}{N_p} R_s I_{\mathrm{PV}}}{N_s N_p \frac{AKT}{q}} \right) - 1 \right] - \frac{V_{\mathrm{PV}} + \frac{N_s}{N_p} R_s I_{\mathrm{PV}}}{\frac{N_s}{N_p} R_p} \tag{1}$$

where:

I_{PV} and V_{PV}	The PV current and voltage
I_0	The diode current
R_s and R_p	The PV array series and parallel resistors
A	The panel ideality factor
q	The electron charge
K	The Boltzmann constant
T	The PV array temperature

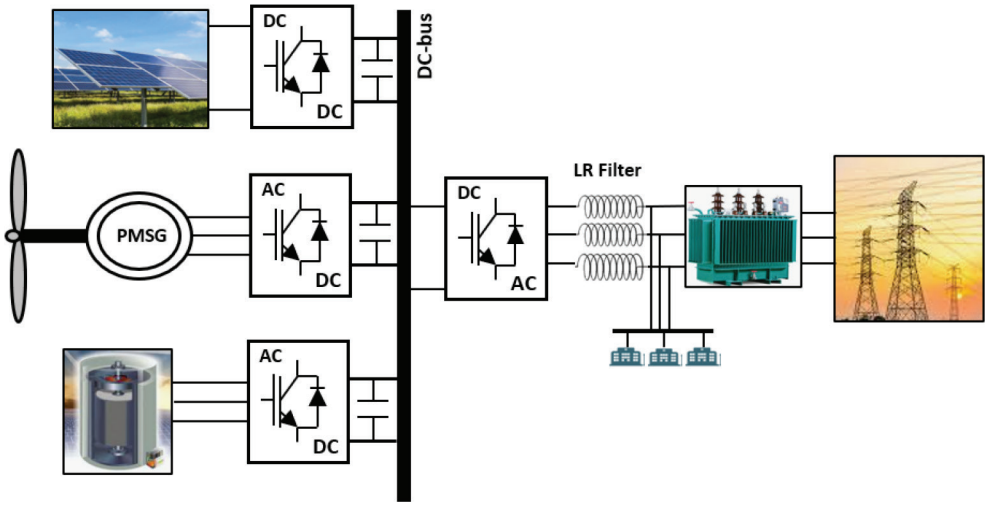

Fig. 1. The architecture of the proposed OG-HRG. OG-HRG, on-grid hybrid renewable generation.

2.3. Modelling of the WT

The WT transforms the kinetic energy of the wind into the mechanical rotational energy of its blades. The mechanical power, P_t, generated by the WT is represented by Eq. (2) (Aloo et al., 2023) as follows:

$$P_t = \frac{1}{2}\rho \mathrm{AC}_p(\lambda,\beta)v_w^3 \tag{2}$$

where:

$A = \pi R^2$	The space covered by the rotor blades (R is the diameter of the turbine blades)
ρ	The density of air
λ	The ratio of the tip speed
β	The angle of the blade pitch
C_p	The WT's power coefficient
v_ω	The velocity of the wind

The tip speed ratio λ of the WT is expressed as shown in Eq. (3):

$$\lambda = \frac{\omega_m R}{v_w} \tag{3}$$

where ω_m is the mechanical angular speed of the turbine rotor.

The turbine power coefficient C_p relies on a complex relationship involving two variables: the tip speed ratio and the blade pitch angle. The power coefficient C_p can be approximated using Eqs (4) and (5) as follows:

$$C_p(\lambda,\beta) = c_1\left(\frac{c_2}{\lambda_i} - c_3\beta - c_4\right).\exp^{\left(-\frac{c_2}{\lambda_i}\right)} + c_6\lambda \tag{4}$$

$$\lambda_i = \left(\frac{1}{\lambda + 0.08\beta} - \frac{0.035}{\beta^3 + 1}\right)^{-1} \tag{5}$$

c_1 through c_6 denote the coefficients related to WT features ($c_1 = 0.5176$, $c_2 = 116$, $c_3 = 0.4$, $c_4 = 5$, $c_5 = 21$, $c_6 = 0.0068$), where λ_i represents the blade pitch angle given in degrees.

2.4. Modelling of PMSG

The mathematical model of PMSG is based on several fundamental assumptions: the three-phase stator windings are symmetrical and distributed sinusoidally throughout the air gap of the machine, the effects of magnetic hysteresis and saturation are not considered and no damping windings are included. In the constructed model, the variables are expressed in the synchronous rotating dq-reference frame, with the *d*-axis aligned to the direction of the flux vector of the permanent magnet rotor. The mathematical equations governing the PMSG are formulated within the conventional dq-reference frame, which rotates in synchronisation with the electrical angular velocity of the rotor. The mathematical model of this system is given in Eq. (6) (Yadav and Balasubramaniyan, 2025) as follows:

$$\begin{cases} v_{sd} = r_s i_{sd} + l_d \dfrac{di_{sd}}{dt} - \omega_e \psi_{sq} \\ v_{sq} = r_s i_{sq} + l_q \dfrac{di_{sq}}{dt} + \omega_e \psi_{sd} \\ \psi_{sd} = l_d i_{sd} + \psi_{\mathrm{PM}} \\ \psi_{sq} = l_q i_{sq} \\ \omega_e = n_p \omega_m \end{cases} \tag{6}$$

where:

v_{sd} and v_{sq}	The dq elements of the stator voltage vector
i_{sd} and i_{sq}	The dq elements of the stator current vector
ψ_{sd} and ψ_{sq}	The dq elements of the stator flux vector
ψ_{PM}	The magnetic field created by the permanent magnets
ω_e and ω_m	The rotor's electrical and mechanical angular velocity of the PMSG
r_s	The resistance of the stator phase
l_d and l_q	The stator inductances for both direct and quadrature components
n_p	The quantity of pole pairs in a PMSG

The electromagnetic torque of the PMSG is expressed in Eq. (7) as follows:

$$T_e = \frac{3}{2} n_p \left(\psi_{sd} i_{sq} - \psi_{sq} i_{sd} \right) \tag{7}$$

The expression for the mechanical motion ω_m of the WT system is represented in Eq. (8) as:

$$T_t + T_e = J . \frac{d\omega_m}{dt} + B_f \omega_m \tag{8}$$

where T_t is the mechanical torque produced by the WT; T_e represents the PMSG's electromagnetic torque, J denotes the overall inertia of the system; and B_f represents the viscous friction coefficient in the mechanical system.

2.5. Modelling of the FESS

A FESS combines a flywheel, a PMSG and an AC–DC converter. This system operates in charging and discharging modes:

- In charging mode, energy is transferred from the DC bus to the flywheel: in this first mode, the PMSG operates as a motor.
- In discharging mode, energy is transferred from the flywheel to the DC bus: in this second mode, the machine operates as a generator.

However, the direction of the current changes depending on the machine's operating mode.
The stored energy E_v in the flywheel is expressed in Eq. (9) (Elkholy et al., 2024) as follows:

$$E_v = \frac{1}{2} J_v . \Omega_v \tag{9}$$

where J_v is the inertia coefficient and Ω_v is the PMSG mechanical speed.

On the other hand, materials with high tensile strength σ_{max} are required to counteract centrifugal forces and enable operation at elevated peripheral speeds. The significant energy content is expressed in Eq. (10) as follows:

$$\frac{E_v}{M} = K \frac{\sigma_{max}}{\rho} \tag{10}$$

With ρ as the material's density, M as the total flywheel mass and K being a constant determined by the flywheel's particular shape.

2.6. Modelling of the DC–DC converter

Typically, the PV system's output voltage V_{pv} is insufficient to meet the DC bus voltage requirement V_{dc}. To bridge this gap, a boost DC–DC converter steps up V_{pv} to the required V_{dc} level. The converter's dynamic behaviour is modelled in Eq. (11) (Chakir and Tabaa, 2024) as follows:

$$\begin{cases} \dfrac{dV_{pv}}{dt} = \dfrac{1}{C_{pv}}\left(I_{pv} - I_L\right) \\ \dfrac{dI_L}{dt} = \dfrac{1}{L_{pv}}\left((D-1)V_{dc} + V_{pv}\right) \\ \dfrac{dV_{dc}}{dt} = \dfrac{1}{C}\left((1-D)I_L - I_{dc}\right) \end{cases} \tag{11}$$

where *D* represents the PWM signal of the boost DC–DC converter.

2.7. Modelling of the DC–AC converter

The grid integration of RESs is achieved through a three-phase inverter that performs DC–AC conversion. The inverter's output voltages (V_{s1}, V_{s2}, V_{s3}), as described by Eq. (12), are directly controlled by the switching signals (k_1, k_2, k_3) that modulate the power devices (Younsi et al., 2022) as follows:

$$\begin{pmatrix} V_{s1} \\ V_{s2} \\ V_{s3} \end{pmatrix} = \frac{V_{pv}}{3}\begin{pmatrix} 2 & -1 & -1 \\ -1 & 2 & -1 \\ -1 & -1 & 2 \end{pmatrix}\begin{pmatrix} k_1 \\ k_2 \\ k_3 \end{pmatrix} \tag{12}$$

To ensure proper grid current injection, an L-type filter (R_f, L_f) interfaces the inverter with the utility grid. The dq axis dynamic model of this filter, derived with (I_d, I_q) as states and (E_d, E_q) as inputs, is formulated in Eq. (13) as follows:

$$\begin{cases} \dfrac{dI_d}{dt} = -\dfrac{R_f}{L_f}I_d + \omega I_q + \dfrac{K_d}{L_f}V_{pv} - \dfrac{1}{L_f}E_d \\ \dfrac{dI_q}{dt} = -\omega I_d - \dfrac{R_f}{L_f}I_q + \dfrac{K_q}{L_f}V_{pv} - \dfrac{1}{L_f}E_q \end{cases} \tag{13}$$

R_f and L_f characterise the grid filter's resistive and inductive components. The grid operates at angular frequency ω, with K_d and K_q serving as the decoupled control inputs for the inverter's dq coordinate frame.

3. Control Strategy of the OG-HRG

The proposed OG-HRG utilises a control strategy that incorporates fuzzy logic control (FLC) for maximum power point tracking (MPPT) to optimise the extraction of PV energy, along with rotor field oriented control (RFOC) to maximise wind energy capture and manage the FESS. To manage the power flow, SMC is employed at the inverter grid interface. Figure 2 illustrates the control strategy of the OG-HRG.

The main purpose of employing both fuzzy logic control and a sliding mode controller together is to establish a robust hierarchical control system. This system optimises energy extraction from the PV array while ensuring that the collected energy is supplied to the grid efficiently, effectively and reliably.

3.1. The PVG FLC-based MPPT

FLC excels in microgrids and real-time systems, offering fast response (<0.5 s) and reliable partial shading performance, though requiring rule tuning. Artificial neural networks (ANN) achieve >99% accuracy in large solar

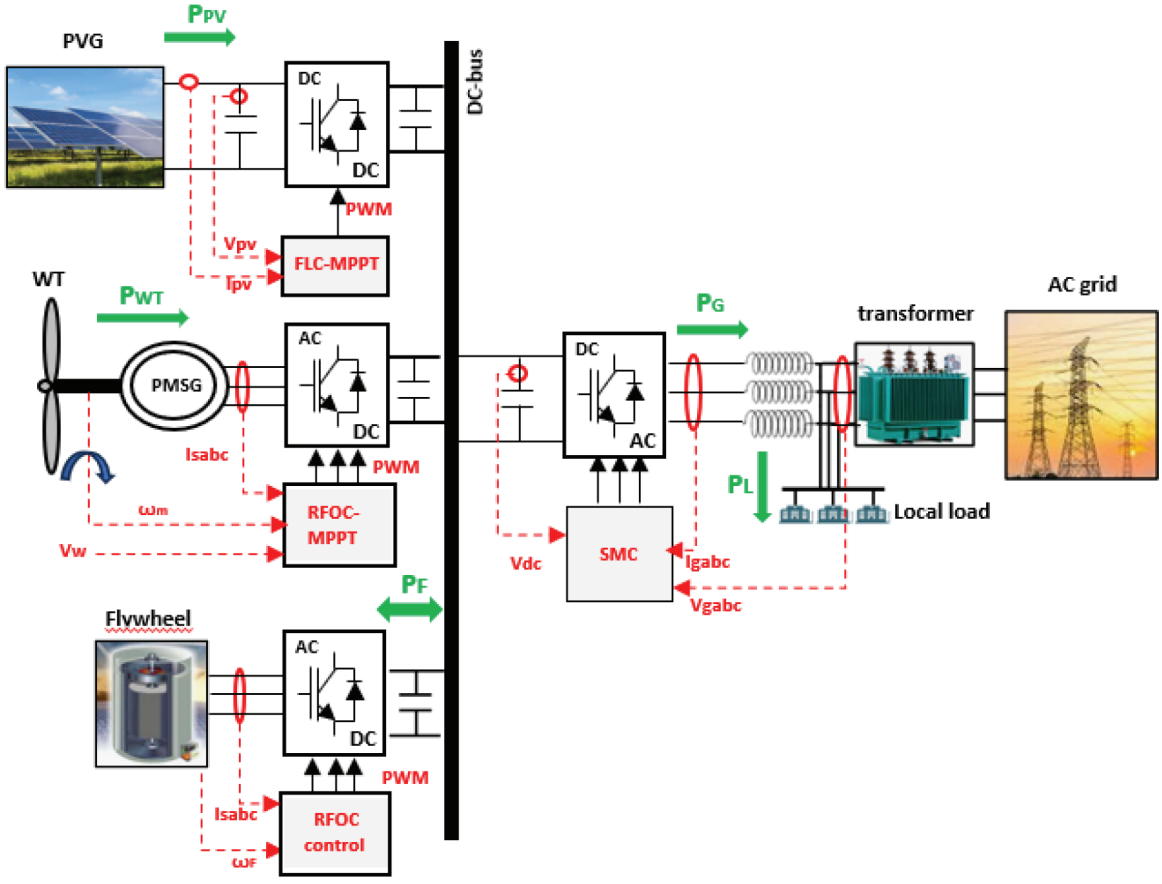

Fig. 2. The control strategy of the OG-HRG. OG-HRG, on-grid hybrid renewable generation; PMSG, permanent magnet synchronous generator; PVG, photovoltaic generator; RFOC, rotor field oriented control; SMC, sliding mode control.

farms but need extensive training data, limiting adaptability (Kaur et al., 2023). Particle swarm optimisation (PSO) suits off-grid systems where its slower convergence (2–5 s) is acceptable, though it struggles with rapid shading changes. FLC balances cost and performance for embedded systems, ANN dominates data-rich environments, while PSO remains a niche for offline optimisation. The choice depends on system needs: speed (FLC), precision (ANN) or flexibility (PSO).

For converting the electrical energy generated by the PV array, a DC–DC boost converter topology is utilised. The schematic for this type of converter is shown in Figure 3.

The FLC-MPPT algorithm optimises PV power extraction by dynamically adjusting the DC–DC converter's duty cycle. It works by sampling PV voltage (V) and current (I) to calculate power (P), computing power (ΔP) and voltage (ΔV) gradients, fuzzifying inputs into linguistic terms (Negative/Zero/Positive), processing through a fuzzy rule base to determine duty cycle adjustments, defuzzifying the output to update the PWM signal and repeating until maximum power point (MPP) is achieved (Pande et al., 2021).

The structure of the FLC strategy is described in Figure 4.

In this study, the inputs of the fuzzy logic controller (FLC) are the slope of the (P_{pv}–V_{pv}) characteristic of the PVG, denoted as E_{pv}(k), and the slope variation $\Delta E_{pv}(k)$ between two time instants k and k−1, which is expressed in Eq. (14) as follows:

$$\begin{cases} E_{pv}(k) = \dfrac{P_{pv}(k) - P_{pv}(k-1)}{V_{pv}(k) - V_{pv}(k-1)} \\ \Delta E_{pv} = E_{pv}(k) - E_{pv}(k-1) \end{cases} \tag{14}$$

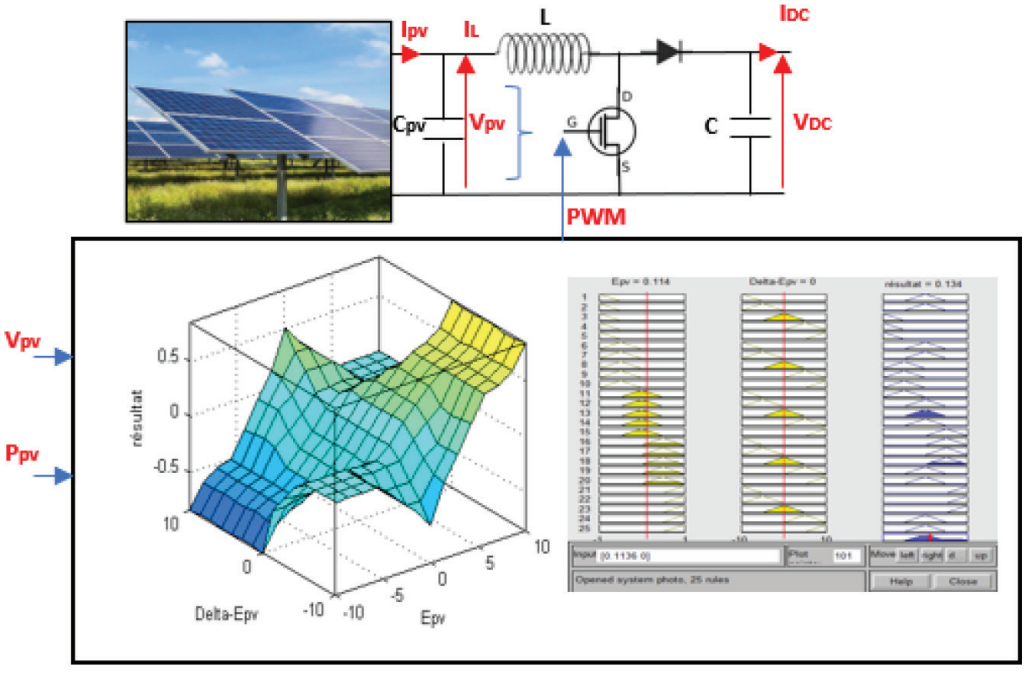

Fig. 3. The configuration of the FLC-based MPPT.

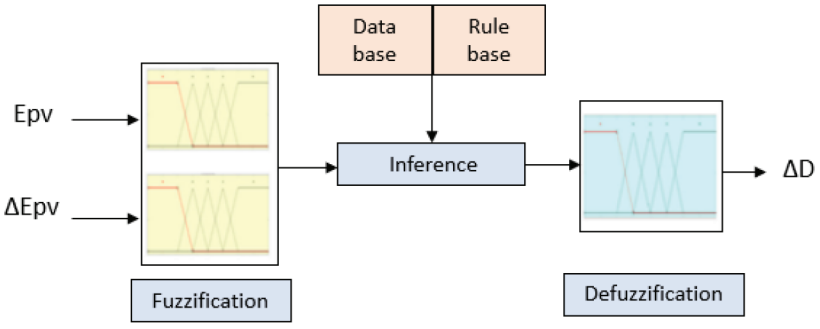

Fig. 4. Structure of the FLC-based MPPT controller.

The fuzzy controller generates outputs ΔD, which are then converted into numerical values, and the duty cycle $D(k)$ is determined using Eq. (15) as follows:

$$\Delta D = D(k) - D(k-1) \tag{15}$$

where $D = 0$ signifies $D(k) = D(k–1)$, which means no variation of the duty cycle.

3.2. MPPT extraction of the WT and rotor field-oriented control of the PMSG

MPPT control determines the turbine's optimal speed by evaluating its power coefficient characteristic $C_P(\lambda,\beta)$, ensuring operation at peak efficiency, establishing the power–speed characteristic curve that correlates the maximum extractable wind power ($P_{t\text{–}m}$) with its corresponding optimal rotor speed ($\Omega_{t\text{–}m}$). C_P designates the power coefficient of the WT, λ refers to the ratio of the tip speed and the blade pitch angle is denoted by β.

The MPPT detects the points where power is at its highest for different wind speeds. The summit of the $C_P(\lambda,\beta)$ curve signifies the greatest amount of power that can be extracted from the wind generator. For low-power uses involving WTs with fixed pitch, the MPPT power regulation is solely handled by the converter control, which modifies the alternator's output parameters, such as current and voltage, influencing the speed of the rotor. The power

coefficient is maximised at this particular β value and a particle speed of λ (λ_m), which is stated in Eq. (16) (Rekioua et al., 2024) as follows:

$$C_P = (0.44 - 0.0167\beta)\sin\left[\frac{\pi(\lambda_m - 3)}{15 - 0.3\beta}\right] - 0.00184(\lambda_m - 3)\beta \tag{16}$$

The maximum value of the $C_P(\beta = 0)$ is given in Eq. (17) as follows:

$$C_{P-m} = 0.44 sin\left[\frac{\pi(\lambda_m - 3)}{15}\right] \tag{17}$$

In this case, the expression for the maximum of the turbine's power is expected as given in Eq. (18):

$$P_{t-m} = 0.5\rho\pi R^5 \frac{\Omega_{m-m}^{\ 3}}{G^3\lambda_m^3} C_{P-m} \tag{18}$$

The expression for the maximum rotation speed of the aerodynamics within the wind speed range from the starting speed to the nominal speed is given in Eq. (19) as follows:

$$\Omega_{t-m} = \frac{V\lambda_m}{R} \tag{19}$$

The corresponding maximum aerodynamic torque is given in Eq. (20) as follows:

$$C_{t-m} = \frac{0.5\rho\pi C_{p-m} R^5}{\lambda_m^3} \Omega_{t-m}^2 \tag{20}$$

3.3. The FESS control strategy

The control scheme for the FESS is shown in Figure 5.

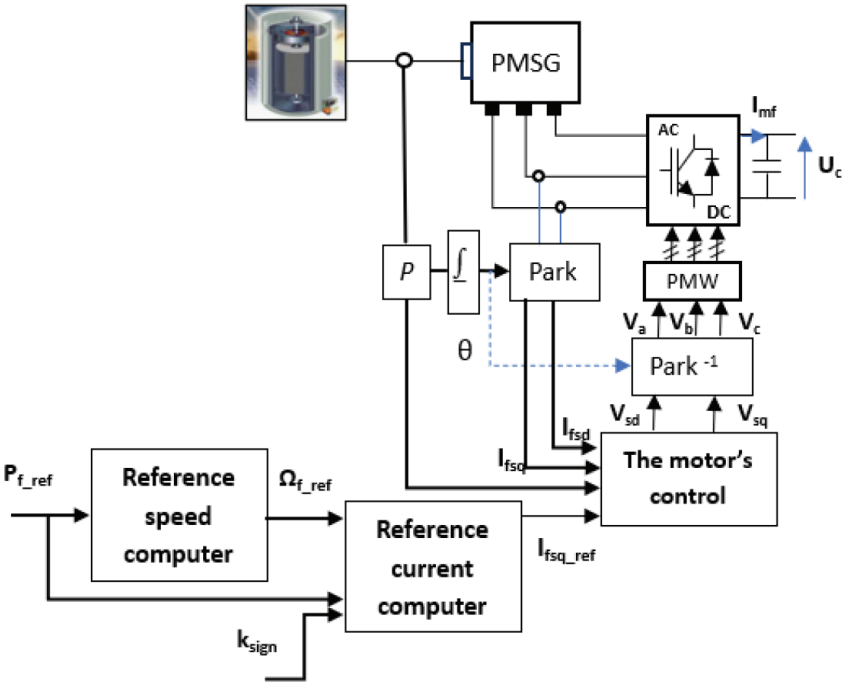

Fig. 5. The control scheme for the inertia-driven energy storage unit. PMSG, permanent magnet synchronous generator.

The reference stator current component on the *q*-axis is expressed in Eq. (21) (Younsi et al., 2023) as follows:

$$I_{fsq\_ref} = k_{sign} \frac{C_{em-ref}}{p.\Phi_m} \tag{21}$$

where C_{em-ref}, p and Φ_m are, respectively, the reference flywheel torque, pole pairs number and the motor flux.

When the storage system is charging, power is transferred from the DC bus to the flywheel (k_{sign} = −1). In contrast, when the storage system discharges, power is transferred from the flywheel to the DC bus (k_{sign} = 1). The standby mode corresponds to k_{sign} = 0. These three operating modes are shown in Figure 6.

The reference speed of the flywheel is determined in Eq. (22) as follows:

$$\Omega_{f\_ref} = \sqrt{\frac{2}{J_f} \cdot E_{c\_ref}^2} \tag{22}$$

Where E_{c_ref} is the reference kinetic energy of the flywheel.

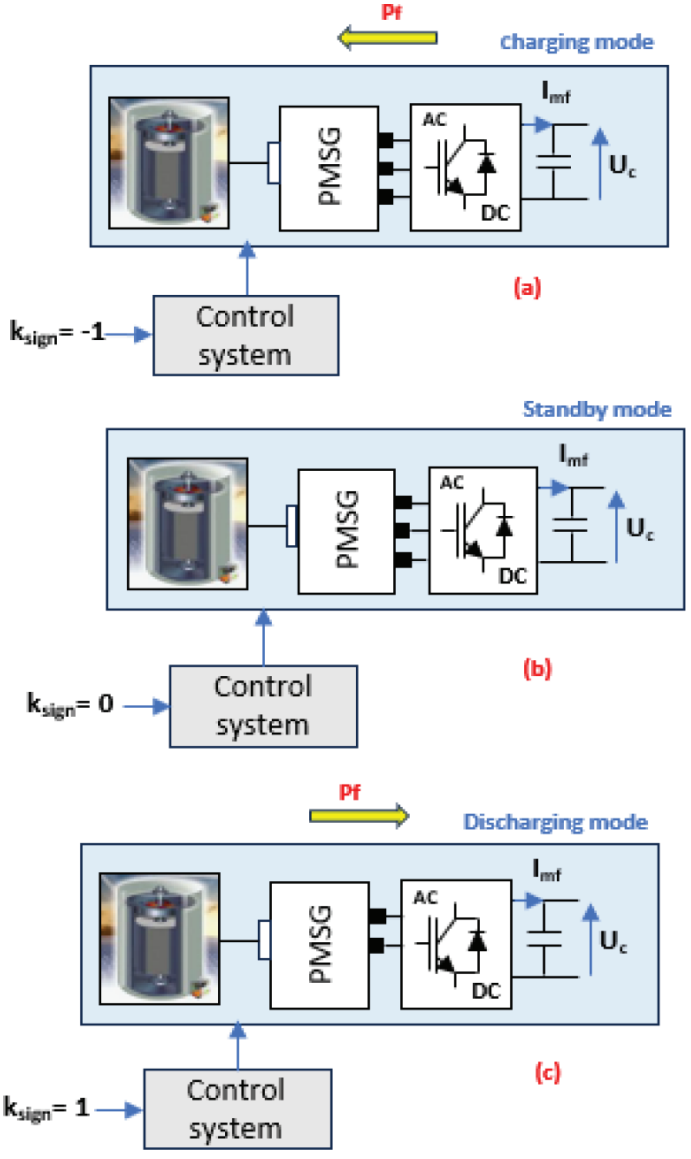

Fig. 6. The FESS operating modes. FESS, flywheel energy storage system; PMSG, permanent magnet synchronous generator.

3.4. The grid-interface SMC

Through SMC, the inverter achieves two primary objectives (Šmídl et al., 2023):

- Maintaining current waveforms with low THD;
- Ensuring precise phase alignment with the grid voltage.

The standard sliding mode controller configuration for this application is depicted in Figure 7.

4. Energy Management Strategy for the OG-HRG

The EMS aims to continuously match the supply from renewable sources with demand from loads and charging/discharging of storage units. The OG-HRG can operate in several scenarios depending on climatic conditions, stored energy, local load demand and network status. This operation improves the system performance in terms of quality of service and security.

The design of the EMS is given in Figure 8.

4.1. The operating modes of the OG-HRG

Table 1 illustrates the different operating modes (Mi) and sub-modes (Mij) of the OG-HRG. Mode M5 produces two sub-modes, which are determined by the direction of power flow from the grid. P_{REN}, P_L, P_F and P_G denote the

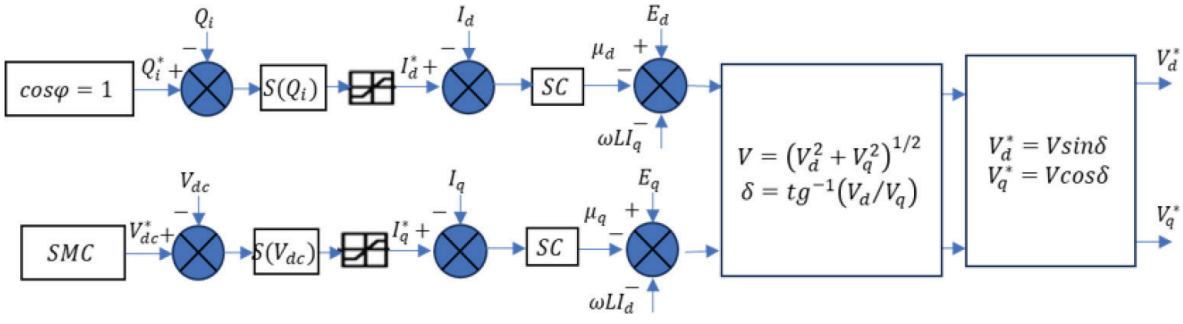

Fig. 7. The architecture of the SMC controller. SMC, sliding mode control.

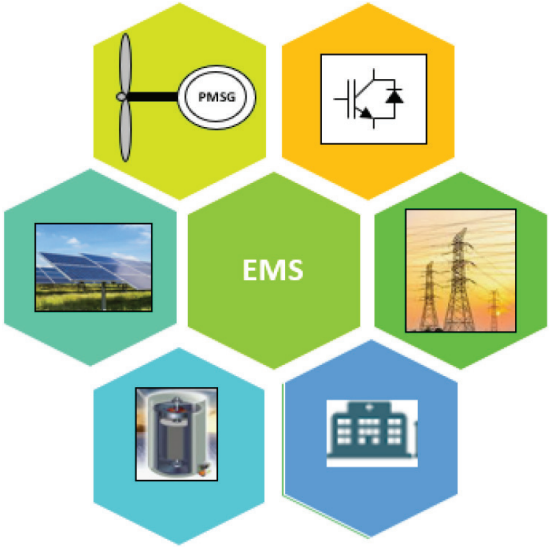

Fig. 8. The EMS of the OG-HRG. EMS, energy management system; OG-HRG, on-grid hybrid renewable generation.

Table 1. The power flow operating modes.

No.	Operating mode	Keys state			Energy movement					Power balance
		K_1	K_2	K_3	E_{REN}	E_G	E_L	E_F	Composition	System state
1	M1	0	0	0	0	0	0	0	Maintenance	----------
2	M2	0	1	1	0	<0	>0	0	Grid-load	$P_G = P_L$
3	M3.1	0	1	0	<0	-	>0	>0	PV + WT—Fl—L (disconnected mode)	Storage: $P_{REN} = P_L + P_F$
4	M3.2	1	0	1	<0	-	>0	<0	PV + WT—Fl—L	Discharge: $P_{REN} = P_L - P_F$
5	M4	1	1	0	<0	0	0	0	PV + WT—grid	Direct injection to grid $P_{REN} = P_G$
6	M5.1	1	1	1	<0	>0	>0	0	PV + WT—grid-load	$P_{REN} > P_L$ $P_{REN} = P_G + P_L$
7	M5.2	1	1	1	<0	<0	0	0	PV + WT—grid-load	$P_{REN} < P_L$ $P_{REN} = P_L - P_G$

PV, photovoltaic; WT, wind turbine.

power generated by the PVG and the WT, the power used by the load, the power exchanged with the flywheel and the power received from or delivered to the grid, respectively. If any system component is disconnected, its power output becomes zero. The energy balance of the system is assessed based on the actions of the two active components of the set-up (RESs and the grid), the storage system and the load status. The availability of a hybrid system component is represented by a logical state (1), while unavailability is indicated by a logical state (0).

Seven scenarios exist based on the state of the power flow, as described in Table 1.

According to Table 1, we identify the following scenarios for energy supply:

- In two operational modes (M3.1, M4) and one sub-operational mode (M5.1), RESs (wind/PV) function as generators while the other components serve as receivers.
- IIn operational mode M3.2, the flywheel operates as a generator.
- IIn operational mode M2, the grid functions as a generator with the RESs disconnected.
- IIn only one sub-operating mode M5.2, energy is simultaneously provided by both sources (renewable energy and the grid).
- IIn operational mode M1, all components of the system are disconnected.

4.2. The EMS strategy

The suggested OG-HRG power management algorithm relies on the subsequent strategy:

If $P_L < P_{REN}$ and the grid is active then:
- The local demand is supplied;
- The grid gets the excess energy.

If $P_L < P_{REN}$ and the grid is inactive (disconnected due to a fault) then:
- The local load is supplied;
- Power is delivered from the DC bus to the flywheel: charging mode.

If $P_L = P_{REN}$ and the grid is active or inactive (islanded mode) then:
- The local load is supplied;
- The grid is not part of the power transfer process;
- No power is exchanged between the bus and the flywheel: standby mode.

If $P_L > P_{REN}$ and the grid is active then:
- The local load is supplied;
- The grid provides the power deficit;
- No power is exchanged between the bus and the flywheel: standby mode.

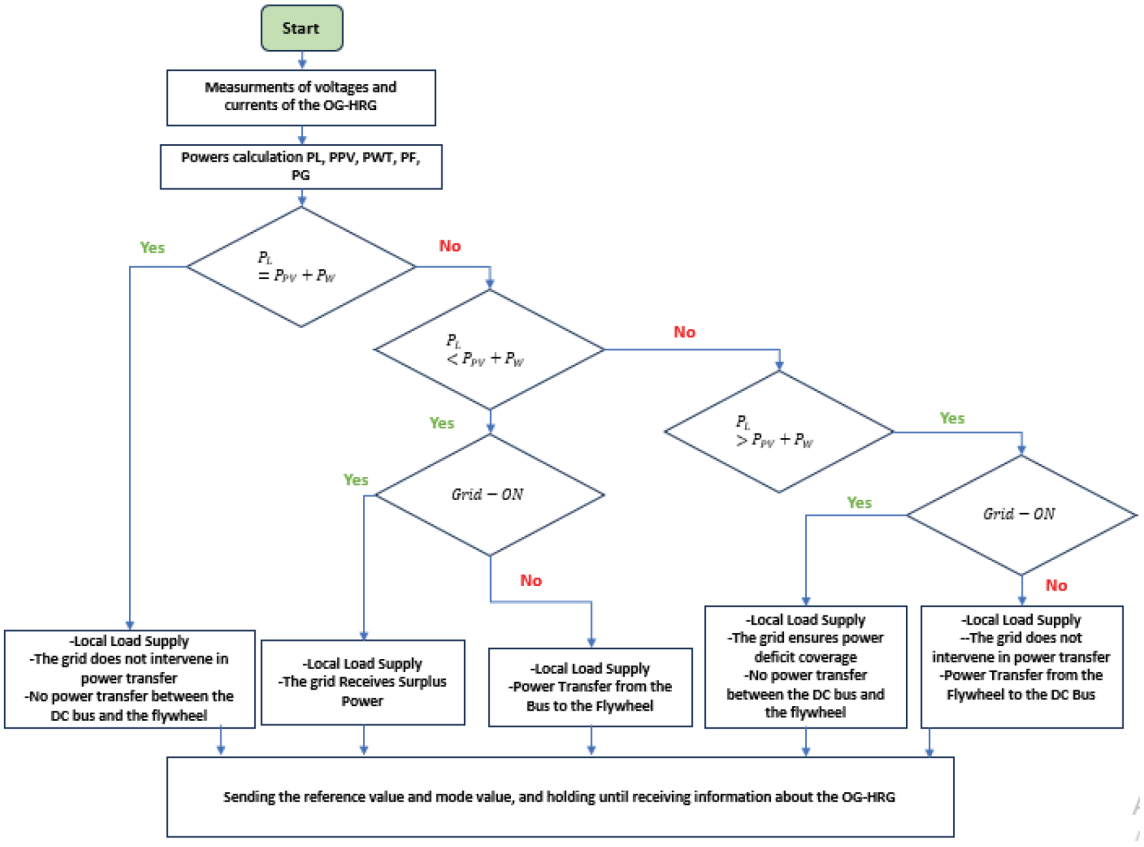

Fig. 9. The flowchart of the EMS of the OG-HRG. EMS, energy management system; OG-HRG, on-grid hybrid renewable generation.

If $P_L > P_{REN}$ and the grid is inactive (disconnected due to a fault) then:

- The local load is supplied;
- The grid is not involved in power transfer;
- Power is delivered from the flywheel to the DC bus: discharging mode.

The flowchart of the EMS is described in Figure 9:

5. Simulation Results and Discussion

In this section, we provide a detailed analysis of a set of graphs that illustrate the various operating scenarios of the overall system. These scenarios are effectively managed through appropriate commands and are continuously monitored by the energy manager. The selected wind profile is illustrated in Figure 10, while the solar intensity is maintained at 600 W/m². During this timeframe, the RES supplies approximately 2,650 W of power.

Additionally, the load profile exhibits variability, as outlined in Table 2. This comprehensive approach enables us to better understand the dynamics of the system and optimise its performance.

Figure 11 illustrates the supplied and absorbed powers of subsystems for the different operating modes. From t = 13.5 s to 15 s, the hybrid system operates in autonomous mode. The network is inactive, and the power supplied by the flywheel is assumed to be sufficient to compensate (absorb) the energy deficit (surplus) during this operating mode, which corresponds to M3.

- Between 13.5 s and 14 s, the power supplied by the RES is approximately 2,650 W, while the load demand is equal to 960 W. The excess power of 1,690 W is sent to the flywheel. The flywheel operates in charging mode (M3.1).

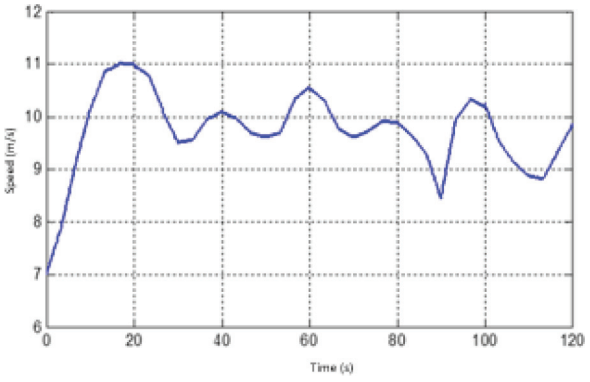

Fig. 10. The wind profile.

Table 2. The power balance for each operating mode.

Operating mode	M3.1	M3.2	M3.1	M5.1	M5.2	M4	M5.1
Time (s)	13.5–14	14–14.5	14.5–15	15–15.5	15.5–16	16–16.5	16.5–17
P_L (W)	960	2,750	960	960	3,960	0	960

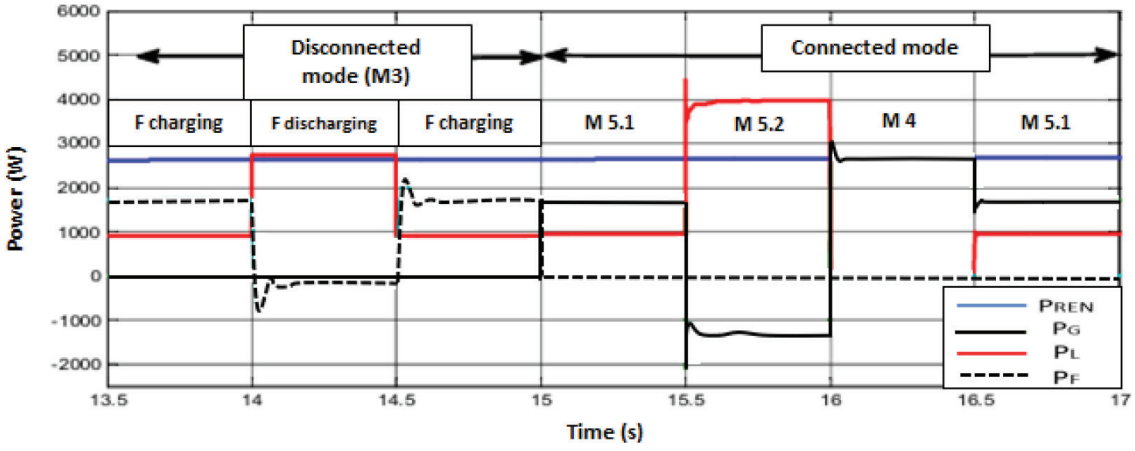

Fig. 11. The powers supplied/absorbed by the subsystems for the different operating modes.

- Between 14 s and 14.5 s, the load demand is around 2,750 W. In this case, the flywheel operates in discharging mode to compensate for the estimated production-consumption power deficit of 100 W.
- Between 14.5 s and 15 s, the load demand drops again to its initial state. The flywheel switches to its charging state to absorb excess power resulting from production and consumption.
- From t = 15 s to 17 s, the hybrid system operates in connected mode. The manager activates the power control of the inverter and the MPPT command on the chopper. The flywheel becomes inactive and does not participate in energy exchange.
- Between 15 s and 15.5 s, the power supplied by the OG-HRG is approximately 2,650 W while the load demand is equal to 960 W. The excess power of 1,690 W is sent to the grid. The system switches to M5.1 mode.
- Between 15.5 s and 16 s, the load demand increases to reach 4,000 W. In this case, and in the absence of the flywheel, the grid compensates for the production–consumption power deficit. The system switches to M5.2 mode.
- Between 16 s and 16.5 s, the load is disconnected, and all of the power generated by the OG-HRG is injected into the electrical grid. The system operates in M4 mode.

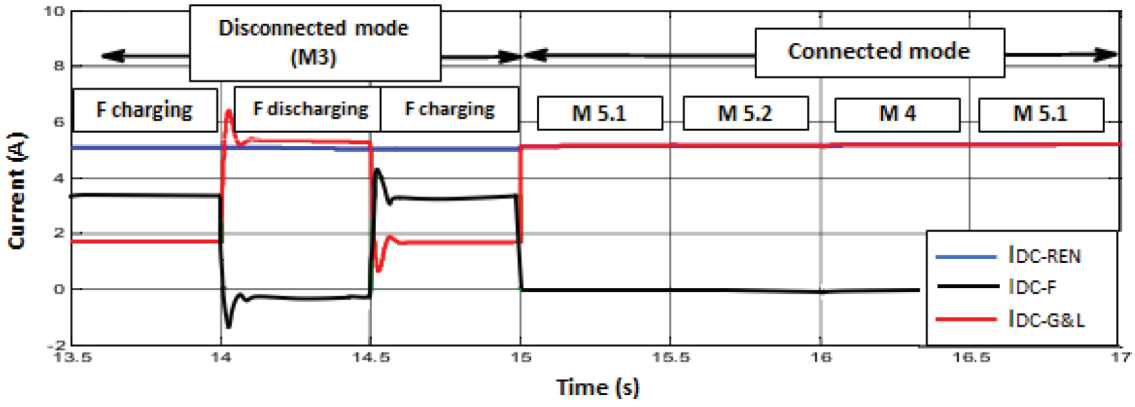

Fig. 12. The variation of currents on the DC bus side.

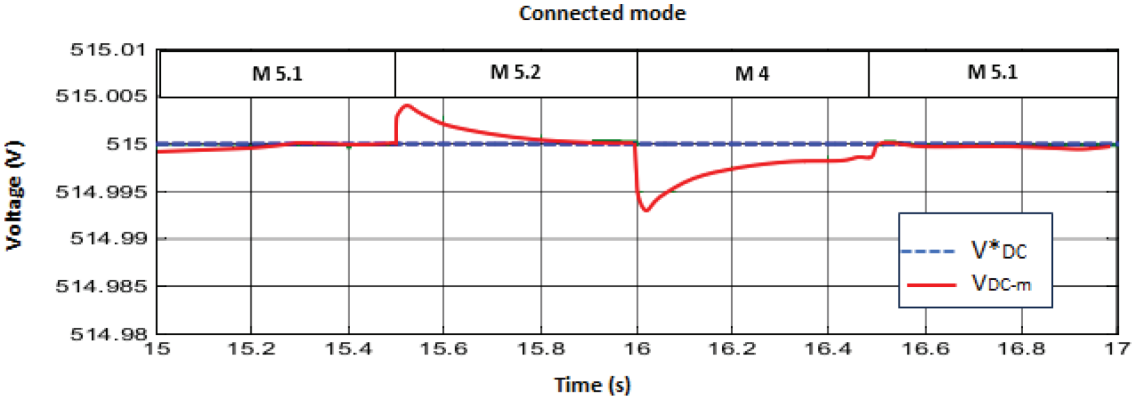

Fig. 13. The variation of voltage on the DC bus side.

- Between 16.5 s and 17 s, the load power becomes 960 W. The power supplied by the OG-HRG is greater than that of the load. However, excess energy is sent to the grid. The system returns to M5.1 mode.

Figure 12 shows the variation of currents on the DC bus side, namely the current supplied by the OG-HRG corresponding to the maximum power, the direct current exchanged with the flywheel, as well as the current at the input of the inverter returned to the load and the grid. The current supplied by the OG-HRG is around 5 A. The current sent or withdrawn from the network depends on the load under the operating modes. In connected mode (M5.1, M5.2 and M4), the current sent to the alternating side presents disturbances each time the operating mode changes. This is due to the nature of the load, which is made up of a pump unit. Figure 13 shows the DC bus voltage, which varies around its reference imposed by the control. However, the simulated voltage deviates from its reference by ±0.005 V each time the operating mode changes. This is due to the start of the load and its temporary nature (asynchronous motor).

For a DC-bus voltage equal to 515 V, the maximum current supplied is around 3.95 A. This current is constant during the different operating modes. In island mode, part of this PV current is consumed by the load (1.75 A) and the balance (2.2 A) is stored in the flywheel to avoid increasing the bus voltage. Figure 14 shows that the bus voltage varies slightly around its reference.

In Figure 15, during the start-up phase, which lasts for 0.5 s, the amplitude of the current at the input of the inverter is of the order of 2.8 A. This current is consumed by the asynchronous motor during starting. Furthermore, the current injected into the flywheel is equal to 1.15 A. At t = 15 s, the inverter connects to the grid since the connection conditions are satisfied. However, the control system switches to power control mode. In this case, the DC bus voltage further converges towards its reference fixed at 515 V. The current returned to the flywheel is cancelled, and that at the input of the inverter goes from 1.7 A to 3.95 A. Part of this current is consumed by the load (1.75 A), and the other part is returned to the grid.

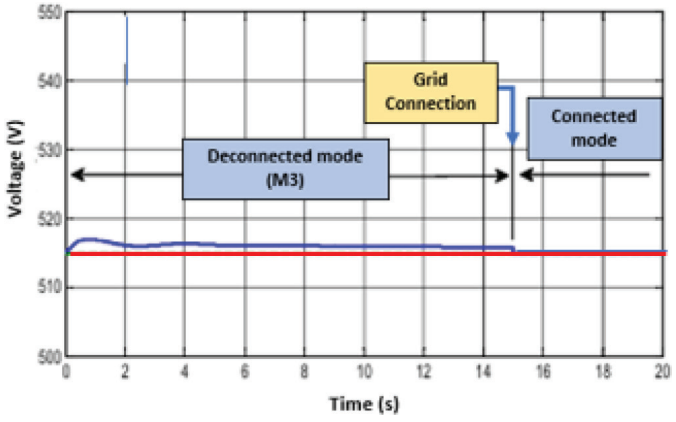

Fig. 14. The DC-bus voltage waveform.

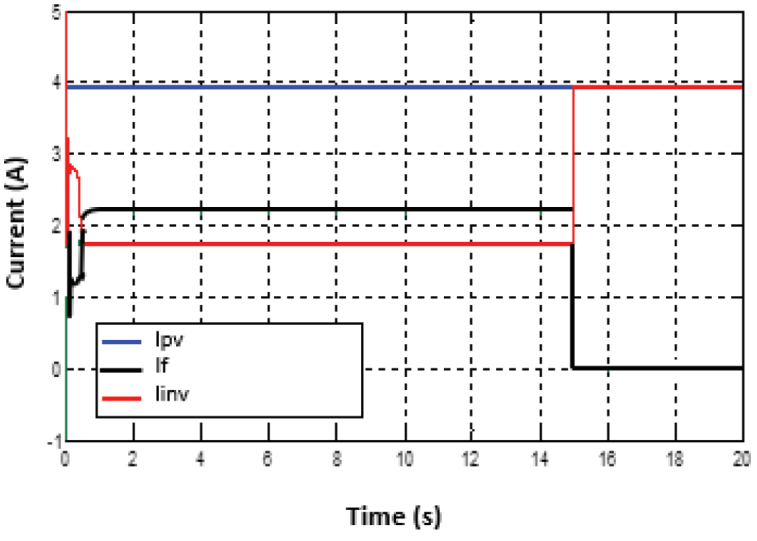

Fig. 15. The PV, Flywheel and inverter current waveforms. PV, photovoltaic.

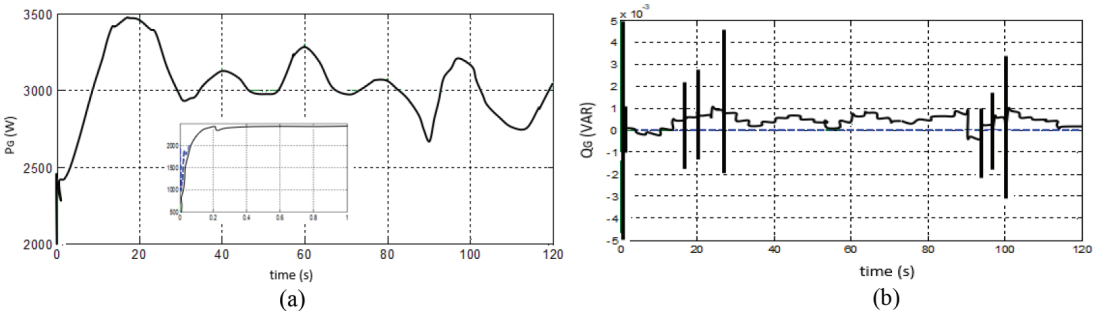

Fig. 16. Profile of the active (a) and reactive (b) power injected into the grid.

The profiles of active and reactive power injected into the grid are shown in Figure 16 ((a): active power P_G and (b): reactive power Q_G).

Figure 17 shows the variation curves of the hybrid system's power in grid-connected and islanded modes >20 s. During these different operational phases, the PV power remains at its maximum (2,040 W) since the MPPT control is not degraded.

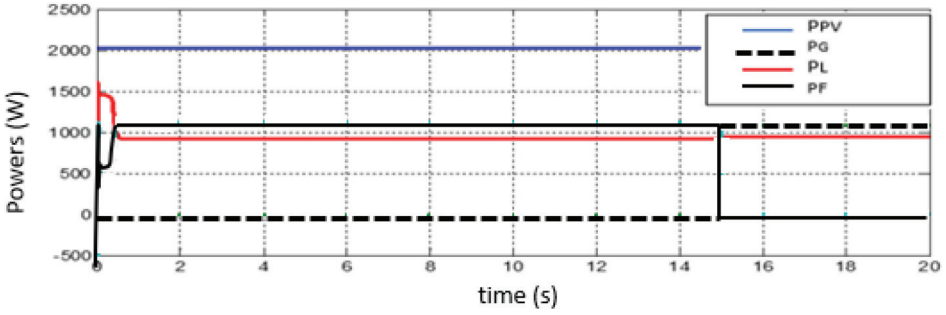

Fig. 17. The power waveforms.

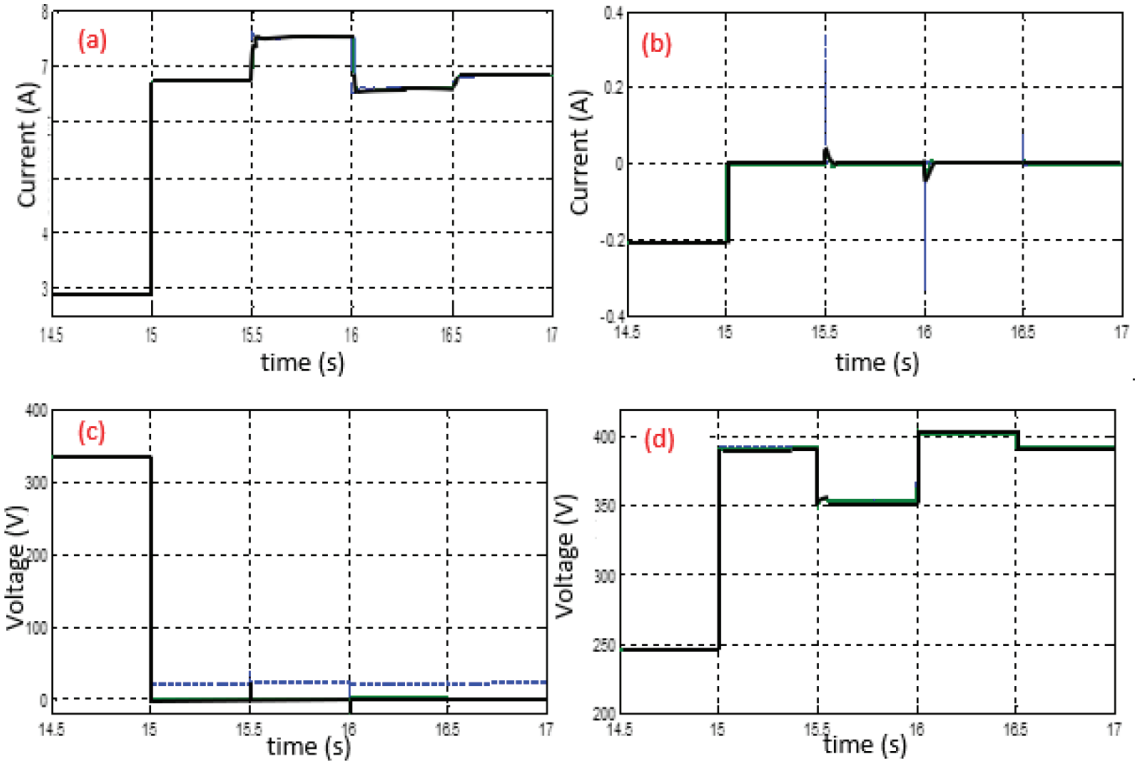

Fig. 18. The direct and quadrature components of the currents and voltages I_d (a), I_q (b), V_d (c) and V_q (d), (simulated and reference) waveforms.

In the islanded mode, which lasts for 15 s, the power injected into the grid is zero, while the power consumed by the load at startup (an asynchronous motor with a rated power of 1 kW) is around 1.5 kW. The surplus power between generation and local consumption is sent to the flywheel (≈600 W). In steady-state operation, the power demanded by the machine is around 950 W, while the surplus (≈1,200 W) is stored in the flywheel.

At the moment of grid synchronisation, the power injected into the flywheel drops to zero, and the power injected into the grid increases from 0 W to 1,080 W. A slight discrepancy in the load power consumption is observed during synchronisation. This discrepancy arises from the transition to a power supply dictated by the grid voltage, which has a slightly higher amplitude than the voltage provided by the inverter in islanded mode.

Figure 18 shows the appearance of the direct and quadrature components of the currents and voltages (simulated and reference) I_d (a), I_q (b), V_d (c) and V_q (d), controlling the inverter for the different operating modes.

The profiles of the output voltage and load current are displayed in Figure 19.

The developed control provides good dynamic performance with regard to voltage and current response. Likewise, it makes it possible to maintain the DC bus voltage constant, whatever the operating mode. In addition, the voltage and current injected by the inverter are always regulated, and the responses follow, without overshoot

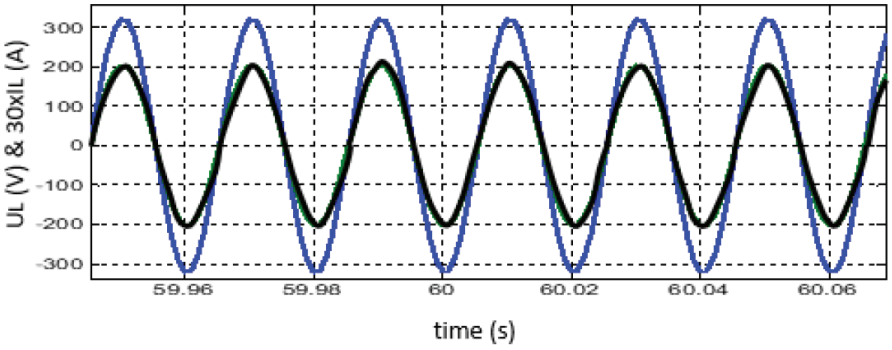

Fig. 19. The load voltage and (30×) load current waveforms.

Table 3. Comparison with other studies.

Paper reference	Energy source and storage	Performance summary
Our paper	Grid-connected PV/wind/flywheel	This system features a multi-layered control approach that combines FLC, PID control and SMC into a unified EMS.
Reference Lata-García et al. (2024)	Stand-alone PV/biomass/diesel/battery	The system consists of a 22 kW solar PV generator, a 1.5 kW biomass generator and a 12 kW diesel generator. Additionally, the battery bank includes 58 units, each with a capacity of 111 Ah, and the dispatch strategy employed is load tracking.
Reference Younsi et al. (2023)	Grid-connected wind/flywheel	This control system includes primary and secondary controllers. The primary stage uses a droop controller to optimise power flow in the resistive network, while the secondary stage employs an improved method to manage voltage and frequency fluctuations during signal disturbances.

EMS, energy management system; PID, proportional-integral-derivative; PV, photovoltaic; SMC, sliding mode control.

and static error, their references generated by the control system. The control system showed notable robustness (accuracy and speed) when varying the load and when switching from one mode to another. Table 3 provides a comparison of the proposed OG-REG with other studies.

6. Conclusion

This paper proposes an analysis and simulation study of an innovative OG-HRG system. The system under consideration includes a gearless WT with a PMSG, a PV array and a FESS. The research concentrated on the DC-coupled architecture of the multi-converter OG-HRG.

The system efficiently manages power flow to loads, adapting seamlessly to the varying operating conditions of RESs. The innovation of the proposed OG-HRG system lies in its integrated analysis, which is more comprehensive than the typical isolated assessments of individual components commonly found in the literature. This holistic approach enables a deeper understanding of the interactions within the system, leading to enhanced performance and stability.

In managing the operation of the PV system, an FLC MPPT algorithm has been applied to achieve the highest possible output of power generated by the PV system under varying conditions of solar irradiation and ambient temperature.

RFOC is applied for the PMSG, integrating the MPPT algorithm to achieve the maximum power generation from the WT. The RFOC is applied to the FESS to manage power flow during charging and discharging phases. The FESS was vital in alleviating power fluctuations and preserving grid stability.

The control of the grid-connected inverter is performed using an SMC approach, which guarantees stable regulation of the DC link voltage and efficient management of the power transfer between the RES and the electrical network. Thus, the incorporation of advanced control techniques guarantees optimal energy extraction and efficient functionality.

The proposed EMS successfully aligned energy production from renewable sources with load requirements and storage demands. The system's performance was assessed under different operational scenarios, showcasing its ability to manage power flow and enhance grid stability.

MATLAB/Simulink simulations demonstrate significant improvements: 72% reduction in power fluctuations compared with battery-based hybrid systems, 85% decrease in CO_2 emissions and operational stability across all seven operating modes (M1–M5.2). This unified approach simultaneously addresses both fast-timescale inertia requirements (via flywheel) and long-term energy balancing needs (through predictive EMS), thereby overcoming the major limitations of existing architectures.

This study highlights the significant potential for further enhancement and optimisation of hybrid renewable energy systems, with a particular focus on energy management strategies and the integration of additional storage technologies. Future research could delve into the scalability of the system for larger grids and the incorporation of diverse RESs. In conclusion, the proposed hybrid renewable energy system, featuring advanced control and energy management techniques, offers a robust solution for sustainable power generation. By blending wind, solar and flywheel storage technologies, this approach provides a reliable and efficient method to address the challenges associated with renewable energy variability, contributing to improved grid stability and more effective energy utilisation. Experimental validation will be addressed in future research.

References

Aloo, L. A., Kihato, P. K., Kamau, S. I. and Orenge, R. S. (2023). Modeling and Control of a Photovoltaic-Wind Hybrid Microgrid System Using GA-ANFIS. *Heliyon*, 9(4), p. e14678. doi: 10.1016/j.heliyon.2023.e14678

Al-Rawashdeh, H., et al. (2023). Performance Analysis of a Hybrid Renewable-Energy System for Green Buildings to Improve Efficiency and Reduce GHG Emissions with Multiple Scenarios. *Sustainability*, 15(9). doi: 10.3390/su15097529

Anvari-Moghaddam, A., Ghaemi, S., You, S. and Blaabjerg, F., eds. (2025). *Power-to-X in Regional Energy Systems: Planning, Operation, Control, and Market Perspectives*, 1st ed. CRC Press. doi: 10.1201/9781032719436

Baala, Y. and Bri, S. (2020). Torque Estimator Using MPPT Method for Wind Turbines. *International Journal of Electrical and Computer Engineering*, 10(2), pp. 1208–1219. doi: 10.11591/ijece.v10i2.pp1208-1219

Bhutto, J. K. (2024). Augmented Two-Stage Hierarchical Controller for Distributed Power Generation System Powered by Renewable Energy: Development and Performance Analysis. *Sustainability*, 16(14). doi: 10.3390/su16145872

Chakir, A. and Tabaa, M. (2024). Hybrid Renewable Production Scheduling for a PV–Wind-EV-Battery Architecture Using Sequential Quadratic Programming and Long Short-Term Memory–K-Nearest Neighbors Learning for Smart Buildings. *Sustainability*, 16(5). doi: 10.3390/su16052218

Dunna, V. K., Chandra, K. P. B., Rout, P. K., Sahu, B. K., Manoharan, P., Alsoud, A. R. and Derebew, B. (2024). Super-Twisting MPPT Control for Grid-Connected PV/Battery System using Higher Order Sliding Mode Observer. *Scientific Reports*, 14(1), pp. 1–17. doi: 10.1038/s41598-024-67083-w

Elkholy, M., Schwarz, S. and Aziz, M. (2024). Advancing Renewable Energy: Strategic Modeling and Optimization of Flywheel and Hydrogen-Based Energy System. *Journal of Energy Storage*, 101(August). doi: 10.1016/j.est.2024.113771

Emon, I. I., Jowel, A. R., Jawad, A. and Nahid-Al-Masood. (2023). Participation of Battery Energy Storage System for Frequency Control in Wind Dominated Power Systems: An Analytical Approach. *Energy Reports*, 10, pp. 1268–1286. doi: 10.1016/j.egyr.2023.08.006

Fernandez, M. I., Go, Y. I., Wong, D. M. L. and Früh, W. G. (2024). Review of Challenges and Key Enablers in Energy Systems Towards Net Zero Target: Renewables, Storage, Buildings, & Grid Technologies. *Heliyon*, 10(23), p. e40691. doi: 10.1016/j.heliyon.2024.e40691

Gajewski, P. and Pieńkowski, K. (2016). Advanced Control of Direct-Driven PMSG Generator in Wind Turbine System. *Architectural Electrical Engineering*, 65(4), pp. 643–656. doi: 10.1515/aee-2016-0045

Hamrouni, N., Younsi, S. and Jraidi, M. (2019). A Flexible Active and Reactive Power Control Strategy of a LV Grid Connected PV System. *Energy Procedia*, 162(April), pp. 325–338. doi: 10.1016/j.egypro.2019.04.034

I.S.C. Committee. IEEE Standard for Interconnection and Interoperability of Distributed Energy Resources with Associated Electric Power Systems Interfaces, February. 2016.

Kaur, G., Upadhyaya, P. and Chawla, P. (2023). Comparative Analysis of IoT-Based Controlled

Environment and Uncontrolled Environment Plant Growth Monitoring System for Hydroponic Indoor Vertical Farm. *Environmental Research*, 222(October 2022), p. 115313. doi: 10.1016/j.envres.2023.115313

Kechida, A., Gozim, D., Toual, B., Alharthi, M. M., Agajie, T. F., Ghoneim, S. M. S. and Ghaly, R. N. R. (2024). Smart Control and Management for a Renewable Energy based Stand-Alone Hybrid System. *Scientific Reports*, 14(1), pp. 1–19. doi: 10.1038/s41598-024-83826-1

Lata-García, J., Zamora Cedeño, N., Ampuño, G., Jurado, F., Swarupa, M. L. and Maliza, W. (2024). Optimization and Evaluation of a Stand-Alone Hybrid System Consisting of Solar Panels, Biomass, Diesel Generator, and Battery Bank for Rural Communities. *Sustainability*, 16(20), pp. 1–13. doi: 10.3390/su16209012

Li, X., Dong, C., Jiang, W. and Wu, X. (2021). An Improved Coordination Control for a Novel Hybrid AC/DC Microgrid Architecture with Combined Energy Storage System. *Applied Energy*, 292(February), p. 116824. doi: 10.1016/j.apenergy.2021.116824

Luukkanen, J., Saunders-Vázquez, A., Majanne, Y. and Korkeakosk, M. (2023). Possibilities and Challenges of Developing A 100% Renewable Electricity System in Cuba. *Ingeniería Energética*, 44(2), pp. 1–11. [Online]. Available at: https://www.redalyc.org/journal/3291/329175581006/html/#B1

Matos, C., Rosales-Asensio, E., Carta, J. A. and Cabrera, P. (2025). Flywheels in Renewable Energy Systems: An Analysis of their Role in Managing Intermittency. *Journal of Energy Storage*, 122(December 2024). doi: 10.1016/j.est.2025.116674

Morales-García, J., et al. (2023). SEPARATE: A Tightly Coupled, Seamless IoT Infrastructure for Deploying AI Algorithms in Smart Agriculture Environments. *Internet of Things (Netherlands)*, 22(November 2022), p. 100734. doi: 10.1016/j.iot.2023.100734

Öhrström, F., Oscarsson, J., Afzal, Z., Dani, J. and Asplund, M. (2025). From Balance to Breach: Cyber Threats to Battery Energy Storage Systems. *Energy Informatics*, 8(1). doi: 10.1186/s42162-025-00499-4

Pande, J., Nasikkar, P., Kotecha, K. and Varadarajan, V. (2021). A Review of Maximum Power Point Tracking Algorithms for Wind Energy Conversion Systems. *Journal of Marine Science and Engineering*, 9(11), pp. 1–30. doi: 10.3390/jmse9111187

Rekioua, D., Mezzai, N., Mokrani, Z., Oubelaid, A., Kakouche, K., Logerais, P. O., Alshareef, M., Bajaj, M., Tuka, M. B. and Ghoneim, S. S. M. (2024). Effective Optimal Control of a Wind Turbine System with Hybrid Energy Storage and Hybrid MPPT Approach. *Scientific Reports*, 14(1), pp. 1–30. doi: 10.1038/s41598-024-78847-9

Roumeliotis, C., Dasygenis, M., Lazaridis, V. and Dossis, M. (2024). Blockchain and Digital Twins in Smart Industry 4.0: The Use Case of Supply Chain-A Review of Integration Techniques and Applications. *Designs*, 8(6), pp. 1–30. doi: 10.3390/designs8060105

Serat, Z., Danishmal, M. and Mohammad Mohammadi, F. (2024). Optimizing Hybrid PV/Wind and Grid Systems for Sustainable Energy Solutions at the University Campus: Economic, Environmental, and Sensitivity Analysis. *Energy Conversion and Management X*, 24(June), p. 100691. doi: 10.1016/j.ecmx.2024.100691

Shafiullah, M., Ahmed, S. D. and Al-Sulaiman, F. A. (2022). Grid Integration Challenges and Solution Strategies for Solar PV Systems: A Review. *IEEE Access*, 10, pp. 52233–52257. doi: 10.1109/ACCESS.2022.3174555

Šmídl, V., Glac, A. and Peroutka, Z. (2023). Time-Optimal Current Control of Synchronous Motor Drives. *Actuators*, 12(1). doi: 10.3390/act12010015

Ullah, Q., Costa Resende, E., Carlos Gomes Freitas, L., Laaksonen, H. and Godoy Simões, M. (2024). Enhancing Voltage Stability of Grid Forming Power Converters based on Model Predictive Controller. *International Journal of Electrical Power and Energy Systems*, 163(October). doi: 10.1016/j.ijepes.2024.110317

Xu, T., et al. (2023). Energy Balance in a Standalone PV Battery Hybrid Generation System on Solar-Powered Aircraft Using the Model Predictive Control Method. *Energies*, 16(17). doi: 10.3390/en16176185

Yadav, V. V. and Balasubramaniyan, S. (2025). Synchronization Stability and Control Strategies for PMSG-Based Wind Energy Systems Under Grid Fault Conditions. *Energy Reports*, 13(January), pp. 6148–6160. doi: 10.1016/j.egyr.2025.05.052

Younsi, S., Kahouli, O., Alsaif, H., Ben Ali, N. and Chaabane, M. (2023). Grid Interface Control of Wind–Solar Generator in Hail Region of Saudi Arabia Using FOPI Controller. *Frontiers in Energy Research*, 11(November), pp. 1–17. doi: 10.3389/fenrg.2023.1309889

Younsi, S., Kahouli, O., Hamrouni, N., Alsaif, H., Aloui, A. and Hamed, S. (2022). Performance Analysis and Multi-Mode Control of Grid Connected Micro Wind–Solar Hybrid Generator in Saudi Arabia. *Journal of Taibah University for Science*, 16(1), pp. 550–565. doi: 10.1080/16583655.2022.2078134